

Key words: dark ages, reionization, first stars - instrumentation: interferometers - methods: data analysis : observational - techniques: interferometric

The radio environment of the 21 Centimeter Array: RFI detection and mitigation

Yan Huang¹, Xiang-Ping Wu¹, Qian Zheng², Jun-Hua Gu¹ and Haiguang Xu³

¹ National Astronomical Observatories, Chinese Academy of Sciences, Beijing 100012, China;
huangyan@bao.ac.cn

² School of Chemical and Physical Sciences, Victoria University of Wellington, Wellington, New Zealand

³ Department of Physics and Astronomy, Shanghai Jiao Tong University, Shanghai 200240, China

Abstract Detection and mitigation of radio frequency interference (RFI) is the first and also the key step for data processing in radio observations, especially for ongoing low frequency radio experiments towards the detection of the cosmic dawn and epoch of reionization (EoR). In this paper we demonstrate the technique and efficiency of RFI identification and mitigation for the 21 Centimeter Array (21CMA), a radio interferometer dedicated to the statistical measurement of EoR. For terrestrial, man-made RFI, we concentrate mainly on a statistical approach by identifying and then excising non-Gaussian signatures, in the sense that the extremely weak cosmic signal is actually buried under thermal and therefore Gaussian noise. We also introduce the so-called visibility correlation coefficient instead of conventional visibility, which allows a further suppression of rapidly time-varying RFI. Finally, we briefly discuss removals of the sky RFI, the leakage of sidelobes from off-field strong radio sources with time-invariant power and a featureless spectrum. It turns out that state-of-the-art technique should allow us to detect and mitigate RFI to a satisfactory level in present low frequency interferometer observations such as those acquired with the 21CMA, and the accuracy and efficiency can be greatly improved with the employment of low-cost, high-speed computing facilities for data acquisition and processing.

1 INTRODUCTION

Rapid progress in low frequency radio astronomy has been made over the last decade. This is primarily driven by the ambitious goal related to exploration of the cosmic dawn and epoch of reionization (EoR). Indeed, the probe of the dark ages, cosmic dawn and EoR will constitute the last frontier for observational cosmology in the era of precision cosmology. One of the most desirable goals is to unveil the history of how and when the universe was illuminated by the first stars/black holes and underwent a transition from its dark to bright phase. Thanks to the 21 cm radiation of neutral hydrogen, the most abundant type of baryonic matter in the early universe, we should be able to receive information about that important epoch of cosmic evolution, though the signal is extremely weak ($\sim 1 - 10$ mK). Yet, the wavelength of the HI 21 cm radiation has been stretched by a factor of $(1+z)$ due to the expansion of the universe. Therefore, if the cosmic dawn and EoR occurred at redshifts between 6 and 27 in terms of current observational constraints (for a recent summary see Koopmans et al. 2015), the corresponding HI hyperfine radiation has already been shifted to 1.5-6 m in wavelength or 50-200 MHz in frequency.

Such a frequency band for us is common because FM radio is broadcast at 88-108 MHz. On one hand, radio experiments that probe the first lights from cosmic dawn and EoR have to work with low frequency radio astronomy if the HI 21 cm radiation is the unique message carrier. On the other hand, man-made radio frequency interference (RFI) will be a disaster in this frequency range. A remote site is the minimum requirement for low frequency radio observations that can be used to investigate the cosmic dawn and EoR.

Technically, current low frequency radio experiments have benefited from the rapid development of information technology and computer science: For example, conventional analog signal communication in radio astronomy has been replaced by high precision digital processing. A large amount of correlation computation and data communication between antennas in radio interferometers can be carried out by advanced, intelligent computers and networks. Massive amounts of data can be easily stored, transferred, shared and analyzed. All of these novel technologies have revolutionized traditional studies in radio astronomy including methods used for global VLBI. Instead of giant dish antennas, a large number of small antenna units can be integrated and combined to form a large collecting area, which can significantly increase the telescope's sensitivity while maintaining a large field of view. Equipped further with smart receivers, precise, high speed analog-to-digital converters, digital multi-beam forming, powerful computers and state-of-the-art data processing techniques, design and construction of radio telescopes are now moving from traditional mechanization and automation to modern digitization and intelligentization. Several new digital radio telescopes that incorporate advanced software have been built and served as the pathfinders or precursors for the ultimate radio telescope, the Square Kilometre Array (SKA)¹, including GMRT², LOFAR³, LWA⁴, MWA⁵, PAPER⁶, etc. In 2004, we began to construct a unique low frequency radio array, the 21 CentiMeter Array (21CMA), with the goal of performing a statistical measurement of the power spectrum of EoR. A total of 10 287 log-periodic antennas were deployed along two perpendicular arms with lengths 6 and 4 km, respectively. We completed the construction in 2007 and upgraded the system in 2010. Sited in the Tianshan Mountains, west China, the array has been collecting data towards the north celestial pole (NCP) region for nearly five years.

One of the major difficulties in current SKA pathfinders or precursors towards the detection of the cosmic dawn and EoR is that the cosmic signal is only 1-10 mK, but strong RFI may still be present at low frequencies even if radio telescopes are placed in remote areas. This is because there exist two types of man-made celestial sources of RFI: (1) FM radio and TV broadcasting scattered by meteor trails and/or aircraft and (2) satellite communications, in addition to system noise. In addition, the radio foreground dominated primarily by the Milky Way is roughly 4-5 orders of magnitude brighter than the signal to be measured. How to mitigate all these RFI and suppress the foregrounds to a desirable level really poses a technical challenge for on-going and planned experiments. If man-made, time-varying RFI and system noise can be well understood and perfectly excised, there are essentially four steps towards the removals of bright foreground for a radio interferometer: First is to reduce the thermal noise through interferometric correlation, and then integrate for a sufficiently long time even to the confusion limit. Second is to identify and subtract all the bright point sources including those from the leakage of sidelobes, through either the conventional Cotton-Schwab CLEAN algorithm (Schwab 1984) or a more advanced approach such as "Peeling" (Noordam 1982). Third is to remove a power-law or smooth component in the frequency domain because the low frequency foreground is dominated by synchrotron radiation which is believed to be spatially and spectrally smooth. It has been shown by recent simulations (e.g. Alonso et al. 2015) that even the blind method without the assumption of a foreground spectrum can yield similar and satisfactory results. Finally, instead of the EoR imaging which will be achieved by a next generation radio interferometer like SKA, we can statistically construct the power spectrum of

¹ <http://www.skatelescope.org>

² <http://www.ncra.tifr.res.in>

³ <http://www.lofar.org>

⁴ <http://lwa.phys.unm.edu>

⁵ <http://www.mwatelescope.org>

⁶ <http://eor.berkeley.edu>

the low frequency sky, which allows us to further “beat down” the sky noise by a factor of $1/N_\ell$, where N_ℓ represents the independent Fourier modes of the targeted field.

Detection and mitigation of RFI is the first and also a key step for current low frequency radio experiments like 21CMA, and the quality and accuracy of the RFI excision critically determines whether our science goals can be eventually achieved. In this work, we present the radio environment report of the 21CMA, demonstrating the various techniques for identification and removals of RFI in the 21CMA observations. Similar radio environment reports on LOFAR, MWA and LWA can be found in Offringa et al. (2013); Offringa et al. (2015) and Henning et al. (2010), respectively. Besides the traditional approach, we mainly concentrate on the statistical analysis of RFI detection, in the sense that both system noise, including sky noise and cosmological signal like EoR behave like thermal noise at low frequencies, and therefore should statistically follow a Gaussian distribution. If we mitigate all the non-Gaussian components, most of the temporal RFI above the thermal noise should be able to be excised. This can be made either in real time or in data post processing, and the accuracy depends sensitively on time and frequency resolution. Moreover, we introduce the so-call visibility correlation coefficient instead of the conventional visibility, allowing a further reduction of the RFI amplitude. Finally, we briefly discuss the removal of the sky RFI introduced by the leakage of sidelobes from off-field strong radio sources.

2 SYSTEM NOISE: RFI IDENTIFICATION

Radio telescopes, when working at low frequencies of $\nu \leq 200$ MHz, are primarily limited by spatial resolution. For example, their effective apertures should be as large as 10 km to achieve an angular resolution of $\sim 1'$. Employment of radio interferometry turns out to be a unique solution to this problem for low frequency observations. To be specific, signal received by the i -th antenna unit in an interferometric array at time t is usually represented by the voltage V_i

$$V_i(t) = G_i \int B_i(s) E(s, t) d^2s + \epsilon_i, \quad (1)$$

where G_i is the system gain, $B_i(s)$ is the spatial response function (or sometimes primary beam) of the antenna, $E(s, t)$ is the electric field of the cosmic signal along direction s and can also be regarded as the Fourier component for a given frequency ν , ϵ_i is the system noise, and the integral should be taken over all directions being observed. Note that all these quantities are a function of ν . The total power that the i -th antenna receives is given by the autocorrelation of Eq.(1)

$$V_{ii}(t) = |G_i(t)| \int B_{ii}(s) |E(s, t)|^2 d^2s + |\epsilon_i|^2, \quad (2)$$

while the cross-correlation of Eq.(1) yields the so-called visibility function

$$V_{ij}(t) = G_i(t) G_j^*(t) \int B_i(s) B_j^*(s) |E(s, t)|^2 e^{i2\pi\nu\Delta t} d^2s + \epsilon_i \epsilon_j^*, \quad (3)$$

in which the raised asterisk indicates the complex conjugate, Δt is the time delay of received signal between the i -th antenna and j -th antenna due to geometric configuration, and the coherence condition of astronomical radiation has already been used. Because noise in two antenna systems is not coherent, the time averaged operation of $\langle \epsilon_i \epsilon_j^* \rangle$ will significantly reduce the noise level, and sometimes the last term in Eq.(3) can even be neglected. Quantitatively, $\langle \epsilon_i \epsilon_j^* \rangle$ is $1/\sqrt{\Delta\tau\Delta t}$ times smaller than the noise power of a single antenna $|\epsilon_i|^2$ or $|\epsilon_j|^2$, where $\Delta\tau$ is integration time and $\Delta\nu$ is bandwidth.

Fig.1 shows a typical example of the total powers of auto- and cross-correlations. Data are taken from 24-hour observations on 2013 May 11 for two antenna pods E01 and E20 along the east-west baseline of 21CMA, separated by 1280 m. (The same data set will be used below unless otherwise stated.) The signal is digitized at a sampling rate of 400 MHz with 8 bit precision. We adopt a frequency channel of 8192, which provides a resolution of 24.2 kHz over a bandwidth of 200 MHz. Fast Fourier transform

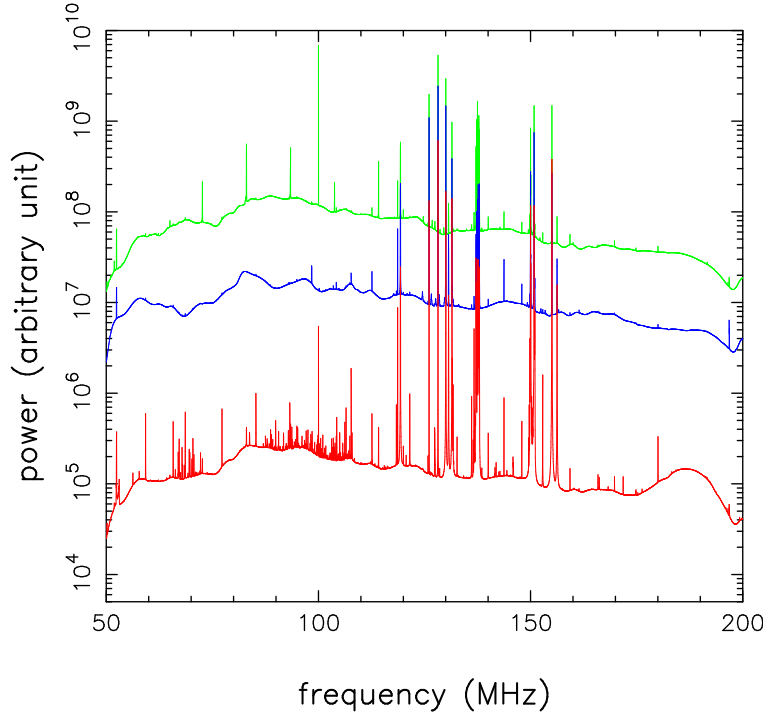


Fig. 1 Average powers of autocorrelation for E01 (blue) and E20 (green) and their cross-correlation (red).

(FFT) and correlation calculations are performed in real time through software, and the digitized and correlated data are integrated for about 3.558 seconds before they are output to a hard disk. A total of 24 280 visibilities including autocorrelations are recorded in each channel for offline analysis. From the average power displayed in Fig.1, we learn that the power or autocorrelation of a single antenna pod is dominated by the system thermal noise $|\epsilon_i|^2$ or $|\epsilon_j|^2$, and V_{ii} and V_{jj} are almost three orders of magnitude larger than the power of visibility $|V_{ij}|$. As mentioned above, thermal noise follows a Gaussian distribution and $\langle \epsilon_i \epsilon_j^* \rangle$ is therefore reduced by a factor of $1/\sqrt{N}$ as compared with $|\epsilon_i|^2$ or $|\epsilon_j|^2$, where N is the total number of samples over an integration time of $\Delta\tau$ and a bandwidth of $\Delta\nu$. This yields $1/\sqrt{N} = 1/\sqrt{\Delta\tau\Delta\nu} = 1/\sqrt{24\text{kHz} \times 3.558\text{s}} = 3.4 \times 10^{-3}$. The actual noise level of $|V_{ij}|$ shown in Fig.1 is slightly higher than this simple estimate because the efficiency of the 21CMA (50%) has not been taken into account.

Because the system temperature is dominated by thermal noise (the receiver noise of 21CMA is about 50 K), only a few strong RFI features above the thermal noise level are present in the autocorrelation spectrum, as shown in Fig.1. However, after the thermal noise is suppressed by three orders of magnitude, the power of visibility seems very noisy, and a glimpse of the spectrum in Fig.1 reveals many strong RFI signatures. Yet, most of them actually arise from time-varying RFI and sparks, and can be easily identified and mitigated. The strong RFI features in $|V_{ij}|$ are identified as follows: (1) Civil aviation communications at 119 MHz and 130 MHz, produced by commercial aircraft which last 4 minutes each time when an aircraft flies over the 21CMA valley. (2) Low earth orbit satellite broadcasting at 137 MHz, generated by the ORBCOMM constellation. The good sky coverage of the ORBCOMM satellites indicates that they are the most prominent RFI source for all low frequency radio telescopes even at remote sites. Furthermore, since there are always several ORBCOMM satellites above the horizon at any given time, the 137-138 frequency band can hardly be used. Yet, they may serve as a beacon for cal-

ibration of our telescopes (e.g. Neben et al. 2015). (3) Walkies-talkies from local train communications at 151 MHz, which often cause the problem of saturation when trains pass through the 21CMA site. As a result, some of the data in the 150-151 band have to be flagged for blanking. Fortunately, the old railroad track at the site is no longer used and the strongest interference at 151 MHz has thus disappeared since January 2014. (4) FM radio broadcasting at 88-108 MHz, which is scattered by meteor trails and aircraft. Note that the site, surrounded by mountains with altitudes over 3000 m, cannot receive FM transmissions from local towns. (5) AM radio broadcast around 70 MHz, which is time variable and rather weak. (6) Computer noise at 100 MHz and 107.7 MHz, which appears occasionally and is sharp but very strong. For the sample (2013 May 11, observation) we chose in this paper, the computer RFI at two narrow bands of 100 MHz and 107.7 MHz remains active through the whole observing time. The source of noise is identified as being due to the synchronization clock used in our other experiment on radio detection of cosmic air showers and cosmic neutrinos (Ardouin et al. 2011).

3 SYSTEM NOISE: STATISTICAL TREATMENT

Most of the RFI shown in Fig.1 is highly varying in time and can be easily detected and mitigated, though the accuracy and efficiency depend on time and frequency resolutions. For example, setting a threshold in visibility may allow us to excise most of the strong RFI. Alternatively, one may use a statistical or automated method to identify RFI in visibility. Note that both system noise (including sky noise) and cosmic radio sources behave like thermal noise, and therefore the visibility data without terrestrial RFI should exhibit a Gaussian distribution. Now, if we identify and remove all the non-Gaussian structures in each channel, RFI should be effectively mitigated. Such an approach can be applied to either data acquisition in real time, if a proper trigger (or standard deviation) is set for each channel, or data post processing. The latter seems more flexible and convenient for users but could result in inaccuracy of RFI detection due to the lack of high time resolution. To guarantee the efficiency of the 21CMA data acquisition which uses software to do FFT and correlations, here we demonstrate the statistical mitigation of RFI only during data post processing.

Fig.2 shows the time variation of the visibility power $|V_{E01W20}|$ for antenna pair E01E20 at a central frequency of 160 MHz and with a bandwidth of 0.1 MHz. If we directly apply Gaussian statistics to the data, we probably need to deal with the problem of large dynamical range. Meanwhile, we also lose the phase information in visibility. Therefore, we begin by normalizing the real and imaginary parts of visibility separately, i.e. dividing by their own mean amplitudes, so that the real and imaginary parts of visibility are both varying around '0'. In Fig.3 we illustrate the normalized real part of the visibility V_{E01W20} versus time. If we excise the data points beyond 5σ , all the strong RFI can be mitigated. Setting a tight limit of 3σ should allow us to exclude most of the RFI yet at the cost of losing or distorting some of the true signal. The choice of the excision limit varies among different experiments. For example, PAPER adopts a limit of 6σ in Pober et al. (2013) and 3σ in Parsons et al. (2014). When processing the 21CMA data, we work with an adaptive choice of the σ range. For the channels that are frequently contaminated, such as 121 MHz, 137 MHz (see Fig.4), and 151 MHz, we adopt a limit of 3σ . Otherwise, we use a more relaxed choice of 5σ (see Fig.3) because the majority of the channels actually remain very quiet. For comparison in Fig.4, we provide an extreme example of the most seriously contaminated case at 137 MHz along with the 3σ and 7σ limits.

With the above RFI detection limit, we can now calculate the RFI occupancy in different frequencies, which provides a quantitative description of the RFI influence on our radio observations. In Fig.5 we display the RFI occupancy spectrum for E01E20. The most contaminated channels are found to be 100 MHz and 107.7 MHz - the sharp noise from the synchronization clock used in our experiment on cosmic rays at the same site, followed by the ORBCOMM satellite signal around 137 MHz with a maximum occupancy of 33%. Some of the channels below ~ 80 MHz seem a bit noisy and only $\sim 90\%$ of the time can be used for observations. Local train communications at 150 MHz lead to 13% of the data that should be excised. Also, there is a slowly varying occupancy ratio of $\sim 2 - 6\%$, spanning a wide range of frequencies from 175 MHz to 200 MHz, which is attributed to the active radio emission region from our Galaxy and will be addressed extensively in Section 5. For comparison, LOFAR and MWA

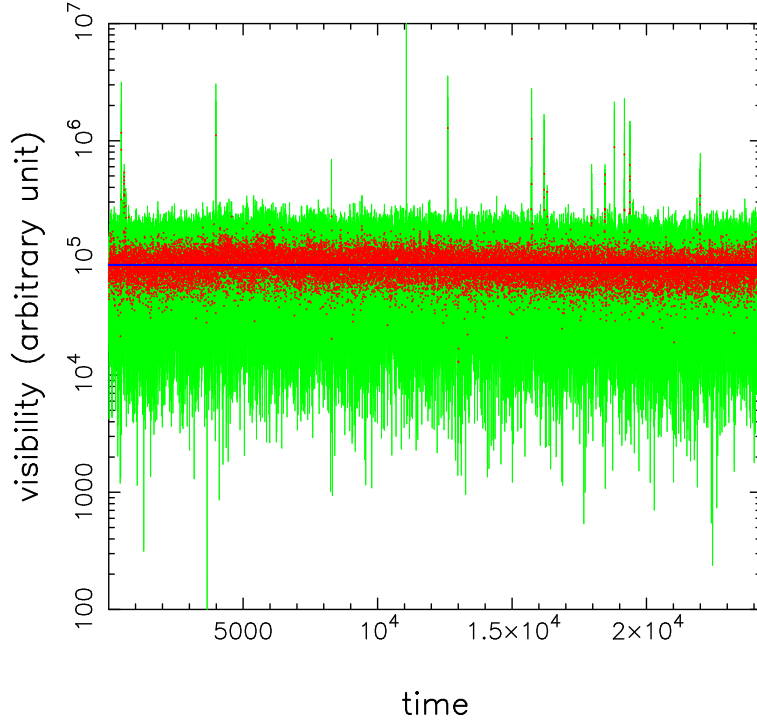


Fig. 2 Time variation of visibility power for the antenna pair E01E20 at a central frequency of 160 MHz with bandwidth 0.1 MHz (four channels). Red points represent the instantaneous average among four channels, while a blue line is the average over an integration time of 24 hours.

have provided their occupancy ratios in a sub-range of 115-163 MHz, which are 3.18% and 1.65%, respectively (Offringa et al. 2013; Offringa et al. 2015). Our result in the same frequency range is 2.66%.

Fig. 6 shows the RFI mitigated power of the visibility V_{E01W20} in terms of the non-Gaussian criterion. As compared with Fig. 1, most of the RFI has been excised or significantly suppressed. It is necessary to make a few remarks on this RFI mitigated visibility power: The overall contour is a convolution of the antenna spectral response with the low frequency radio sky dominated by the Milky Way. The decreasing power with increasing frequency in 85-200 MHz just represents the Galactic radiation, while the turnover near 85 MHz reflects the inefficient antenna gain at lower frequencies. Actually, the design of the 21CMA log-periodic antenna is only optimized for 70-350 MHz. Finally, the rapid attenuation at the two frequency ends arises from the roll-off of the two bandpass filters used in our receiver. In principle, the data from adjacent channels should be excluded.

Even after the temporal RFI is mitigated, system noise still dominates the visibility function at low frequencies, and a long integration is required to “beat down” noise that mainly comes from the Milky Way. For experiments toward the EoR detection, integrating observations may take up to a few years. Therefore, it is crucial to check whether and how the system noise goes down with integration time. Telescope sensitivity in terms of flux can be written as $2k_B T_{\text{sys}} / A_{\text{eff}} \sqrt{t \Delta\nu}$, where k_B is the Boltzmann constant, T_{sys} is the system temperature, and A_{eff} is the effective area of the telescope. In our case, all antenna pods have the same effective area, and their receivers have roughly the same system temperature. It turns out that theoretically, for a given frequency bandwidth, the sensitivity should vary with integration time as $t^{-1/2}$. In Fig. 7 we plot the average visibility power $|V_{E01W20}|$ and its variance

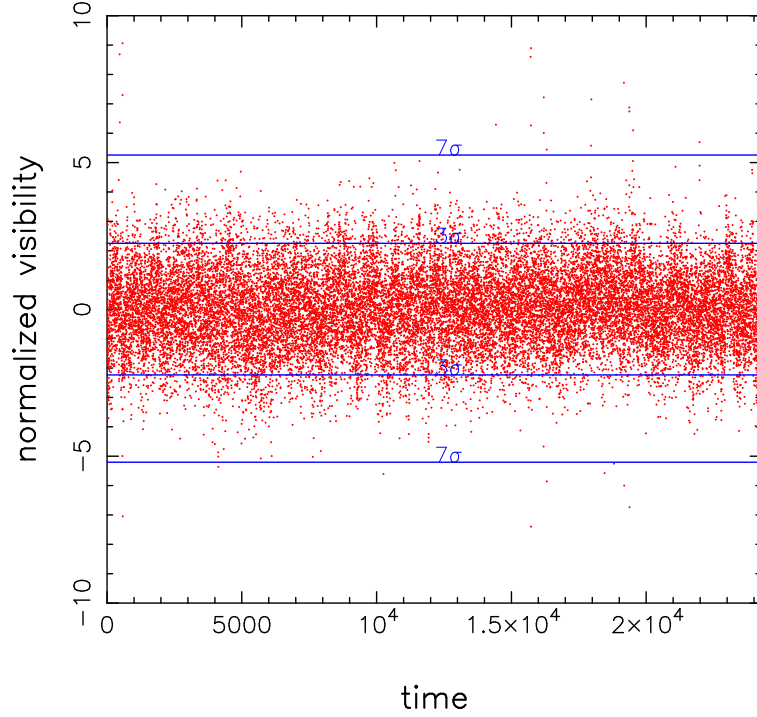


Fig. 3 The real part of the normalized visibility V_{E01W20} versus observing time at frequency $\nu = 160$ MHz.

at $\nu = 160$ MHz against integration time for observations spanning over 24 hours. It appears that the sensitivity does follow the $t^{-1/2}$ behavior. Similar tests have also been made for other EoR experiments such LWA, MWA, etc. (Bowman et al. 2007; Henning et al. 2010; Taylor et al. 2012; Offringa et al. 2015).

4 VISIBILITY CORRELATION COEFFICIENT

We may take a step further to introduce the so-called visibility correlation coefficient in the analysis of RFI mitigation. The visibility correlation coefficient is defined as

$$p_{ij}(t) = \frac{V_{ij}(t)}{\sqrt{|V_{ii}(t)||V_{jj}(t)|}}. \quad (4)$$

We begin with two extreme cases to demonstrate the advantage of utilizing p_{ij} instead of V_{ij} : (1) If the visibility and autocorrelations are dominated by RFI, then the above expression reduces to $p_{ij}(t) = \epsilon_{ij}(t)/\sqrt{|\epsilon_{ii}(t)||\epsilon_{jj}(t)|}$. All strong RFI in antenna unit i and/or j can cancel each other through the $|p_{ij}(t)|$ operation. Namely, p_{ij} can suppress the amplitude of strong RFI as it appears simultaneously in the numerator and denominator. (2) If the noise terms ϵ_{ii} , ϵ_{jj} and ϵ_{ij} are negligibly small, then the power of p_{ij} can be converted into the angular power spectrum C_ℓ through $C_\ell = I_0^2 |p_{ij}(\ell/2\pi)|^2$ (Zheng et al. 2012), in which I_0 is the mean brightness of the observed radio sky. In other words, p_{ij} provides a simple way to statistically measure the angular power spectrum.

Yet in reality, system thermal noise ϵ_{ij} including the Milky Way contribution is comparable to the total flux of cosmic radio sources at frequencies below 200 MHz. Namely, $\langle G_i G_j^* \int B_i(s) B_j^*(s) |E(s)|^2 e^{i2\pi\nu\Delta t} d^2s \rangle$ and $\langle \epsilon_i \epsilon_j^* \rangle$ have the same order of magnitude, unless there

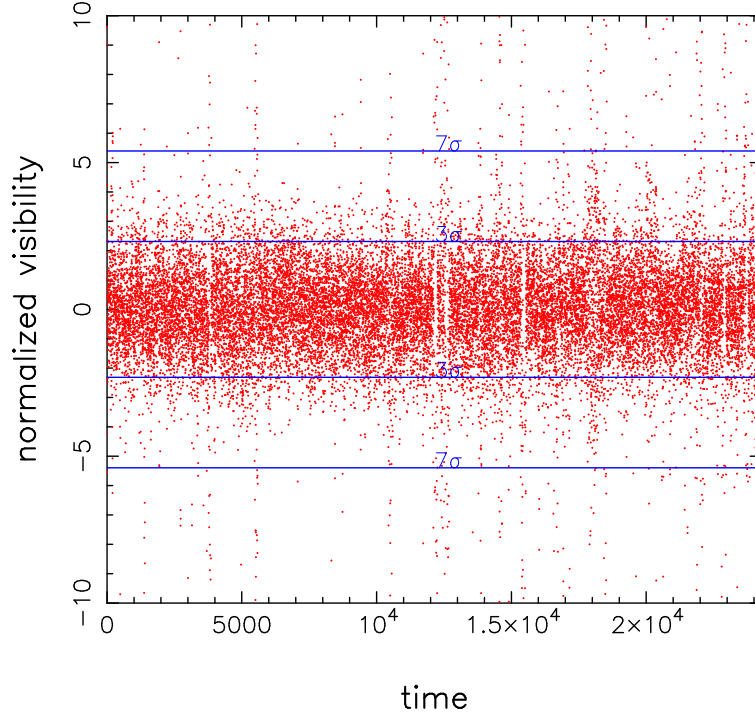


Fig. 4 The same as Fig.3 but for $\nu = 137$ MHz.

is strong RFI in ϵ_{ij} . Indeed, this is supported by the following argument: The Galactic radiation is the main source of noise in current EoR experiments if the receiver noise is controlled within ~ 50 K. The surface temperature of the Milky Way can be estimated by $T_b = 200\text{K}(\nu/150\text{MHz})^{-2.5}$. Its rms variation through the $\langle \epsilon_i \epsilon_j^* \rangle$ operation is modulated by a factor of $1/\sqrt{\Delta\nu\Delta\tau}$: $\Delta T_b = T_b/\sqrt{\Delta\nu\Delta\tau}$. For the EoR experiment like 21CMA, ΔT_b is approximately a factor of 1000 smaller than T_b . Converting ΔT_b into the rms variation in flux yields

$$\Delta S = 0.9\text{Jy} \left(\frac{\lambda}{3\text{m}} \right)^{-2} \left(\frac{\Delta T_b}{0.1\text{K}} \right) \left(\frac{\theta_b}{10^\circ} \right)^2, \quad (5)$$

where θ_b is the width of the telescope primary beam. This simple estimate indicates that the system noise is roughly on the same order of magnitude as the bright radio sources (0.1 Jy - 10 Jy) in the sky. Only when RFI is brighter than the sky noise ΔT_b , i.e., the RFI plays a dominant role in $\langle \epsilon_i \epsilon_j^* \rangle$ and is also greater than $\langle G_i G_j^* \int B_i(s) B_j^*(s) |E(s)|^2 e^{i2\pi\nu\Delta t} d^2s \rangle$, does the employment of p_{ij} become useful and efficient in mitigation of RFI. Although it may be rather difficult to identify weak RFI that is buried under sky noise, it is always helpful to utilize the visibility correlation coefficient for an efficient detection and mitigation of strong RFI.

Now we demonstrate the effect and result of RFI mitigation in terms of p_{ij} for the 21CMA data. There are two ways to employ p_{ij} in data processing: First is to compute p_{ij} from visibility V_{ij} and antenna powers V_{ii} and V_{jj} in data post processing, and work with p_{ij} instead of V_{ij} in subsequent image processing. Second is to add a new task of computing and integrating p_{ij} to the data acquisition phase in real time. The former does not add any extra work in the data acquisition system, but the RFI detection may be affected by poor time resolution in output visibility for which integration has already been done. The latter can maximally guarantee the accuracy of RFI identification and mitigation, at

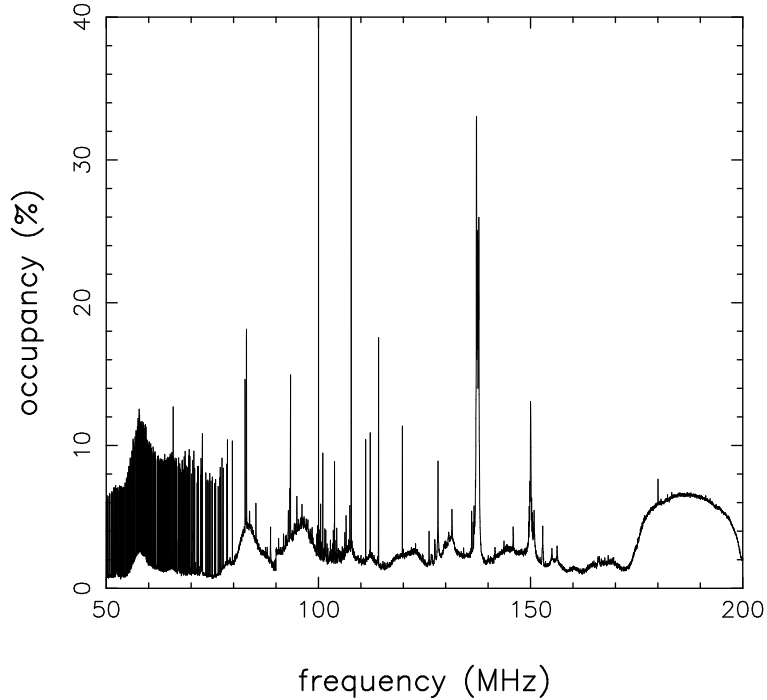


Fig. 5 RFI occupancy spectrum for E01E20, in which RFI is selected in terms of 5σ .

the cost of decreasing the efficiency of data acquisition, because more CPU/GPU time is required to compute p_{ij} and even complete the real-time RFI detection before integration and output operations. Leaving the first approach to data post processing, we tested the second approach with 21CMA during September, 2012. A total of 26 days were devoted to the measurement of p_{ij} instead of V_{ij} , for which the telescope efficiency is found to further decrease by 22%, in addition to the 50% efficiency in its routine observing mode. In Fig.8 we compare the visibility power $|V_{ij}|$, correlation coefficient $|p_{ij}|$ in data post processing and $|p_{ij}|$ at real time, in which the first two results are based on the 2013 May 11 observation, and the third one is taken from the 2012 September 19 measurement. In both case, the same baseline E01E20 is chosen. We take a frequency channel at $\nu = 102$ MHz with a 0.1 MHz bandwidth for the purpose of illustration, because the channel is occasionally contaminated by FM radio signals scattered by meteor trails and/or aircraft. A visual inspection of Fig.8 reveals that the amplitudes of strong RFI in $|p_{ij}|$ become smaller than those in $|V_{ij}|$. To quantitatively evaluate the effect of RFI detection from the three methods, we calculate their mean values \bar{V} or \bar{p} and variances σ . Furthermore, we utilize σ/\bar{V} or σ/\bar{p} to characterize the extent of their dispersion and show the results in Fig.9. It appears that the visibility function suffers from the most serious contamination as indicated by the largest dispersion in σ/\bar{V} , though most of these RFI are actually time-varying or sparks. Note that the same data are displayed in a different way in Fig.1. On the contrary, $|p_{ij}|$ can significantly suppress the effect of RFI, as manifested by much smaller dispersion in σ/\bar{p} . It seems that the real-time operation of $|p_{ij}|$ yields an even better result. If we take into account the fact that the real-time computation of p_{ij} reduces the efficiency of data acquisition to some extent, the data quality of σ/\bar{p} can be further improved with the employment of high-speed computers or field-programmable gate arrays (FPGAs) for FFT and correlations.

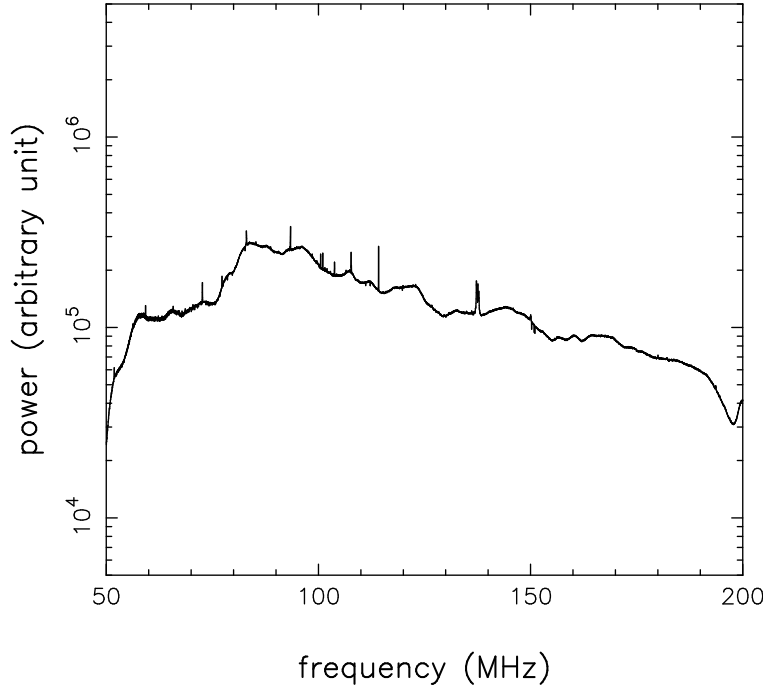


Fig. 6 Average power of the visibility V_{E01W20} after mitigating the non-Gaussian features. See Fig.1 for the original data.

5 RFI IN THE SKY

Unlike the man-made, terrestrial RFI that we have discussed above, celestial RFI is actually emitted by strong radio sources in the sky. But for the EoR experiments at low frequencies, they can also be treated as a sort of RFI and should be mitigated. The dominant radio source in the low frequency sky is of course the Milky Way, and its global, uniform radiation has already been included in the noise term ϵ above. Now, what we will deal with is the structured components that can be captured by radio interferometers, including both Galactic and extragalactic strong radio sources.

Fig.10 is the waterfall plot for the real part of visibility V_{E01E20} observed on 2013 May 11, which illustrates the 24 hour variation in the radio environment containing both terrestrial RFI and celestial sources. Three predominant features from the sky are identified as follows: (1) Thick fringes; these correspond to the brightest radio source (quasar) within 1 degree of NCP, B004713+891245, with a flux of 5 Jy and flat spectral index. (2) Thin fringes; these are generated by the brightest radio galaxy, 3C061.1, located ~ 4 degrees from NCP. Extrapolating its spectral index of -0.8 to 150 MHz, we find that it has a flux of roughly 33 Jy. (3) Two bright spots with noticeable fringes and an interval of 6 hours, which are the strongest RFI source in the 21CMA NCP field and will be the main focus in this section. Actually, we have already seen their effect through the bumps at $\nu = 175 - 200$ MHz shown in Figs.1, 5 and 9. For the two bright extragalactic sources, B004713+891245 and 3C061.1, we will include them in the source catalog observed with 21CMA and present their properties and excision elsewhere (Zheng et al. 2016).

In order to understand the origin of the two strong RFI features around 180 MHz with interval time of 6 hours, we begin with the beam pattern of the 21CMA pod. Each of the 21CMA pods consists of 127 log-periodic antennas which are combined through a phase delay cable to form an analog beam towards NCP. The primary beam, centered on NCP, has a field of view of approximately $8.5^\circ(\nu/100\text{MHz})^{-1}$.

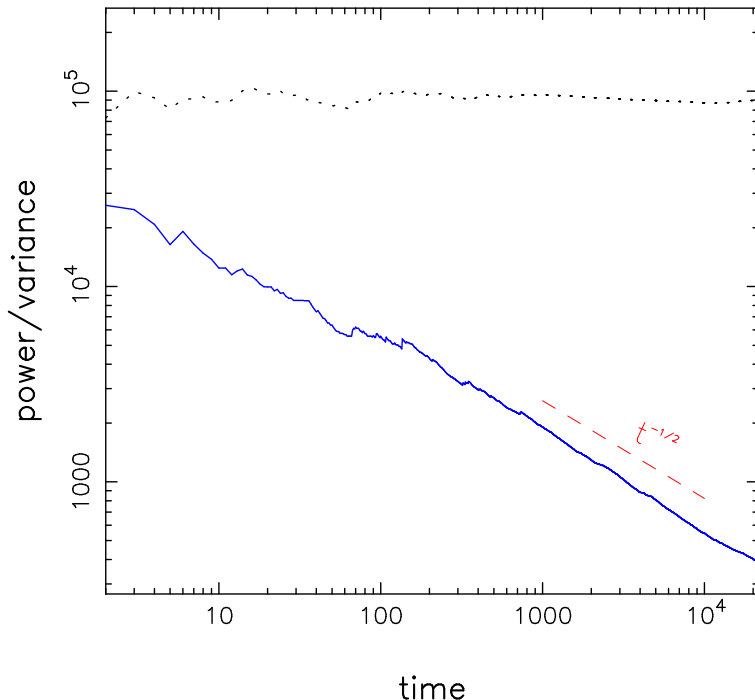


Fig. 7 Average visibility power $|V_{E01W20}|$ (black) and its variance (blue) at $\nu = 160$ MHz versus integration time. The latter continues to drop as $t^{-1/2}$ over 24 hours.

However, the regular spacing of 127 antennas in the hexagonal pod also leads to two remarkable sidelobes, separated by 90 degrees with respect to the NCP. Their radii vary with frequency, and reach about 45° near $\nu = 175 - 190$ MHz. In Fig.11(a) and Fig.12(a) we display the beam patterns of 21CMA for $\nu = 150$ MHz and $\nu = 180$ MHz, respectively. If no radio sources fall into the sidelobes during diurnal motion of the heavens, then our observation towards the NCP field is unaffected by existence of the sidelobes. Otherwise, the sidelobe leakage of off-field radio sources may contaminate our observation and should be removed. Unfortunately, as the dominant source of radio emission at low-frequencies, the Galactic plane sweeps the NCP region every 24 hours, which brings the Galactic emission into the 21CMA field of view twice per day through the two sidelobes. In particular, a large star forming region called Cygnus A is just located about 45° from NCP, and can be clearly seen through the two sidelobes of the 21CMA at frequencies around 180 MHz. This gives rise to the two bright spots, separated by exactly 6 hours, in the waterfall plot shown in Fig.10. These regions that cause contamination will be a disaster for our interferometric imaging of the EoR sky and should certainly be excised. On the other hand, the sidelobe leakage may provide a way to study the large star forming region in Cygnus, e.g., by monitoring of time variation using long integration data of the EOR spanning years.

Now we discuss very briefly another type of RFI from the sky due to the grating sidelobes of the 21CMA. Except for the easternmost pod at a distance of 4646 m from the center of the east-west arm, the other 80 pods that compose the 21CMA are not randomly deployed along the two baselines. Spacings between pods are integral multiples of 20 m for both east-west and north-south arms. As a result, there are only 212 independent baselines among the total 3240 instantaneous ones. While the numerous redundant baselines are useful for the purpose of self-calibration and measurement of the EoR power spectrum (e.g. Noordam & de Bruyn 1982; Tegmark 2010), they also generate the so-called grating sidelobes (Bracewell & Thompson 1973; Amy & Large 1990). These equally spaced rings have

their spatial responses almost comparable to that of the main lobe, causing serious contamination to our observation if they happen to 'see' the Galactic and extragalactic radio sources. For example, the two brightest radio sources in the sky, Cas A and Cygnus A, would both show up in the 21CMA field due to the grating sidelobes. All these troublespots for our EoR experiment should be CLEANed either from ungridded visibilities through a proper modeling of the sky or in image processing.

Using real 21CMA real observations, we have thus far discussed the detection and mitigation of both time varying, terrestrial RFI and the time-invariant, celestial RFI. The next step is to move on to interferometric imaging, which, however, exceeds the scope of the present paper. The details of this can be found in Zheng et al. 2016. For illustration, we show in Fig.13 and Fig.14 the RFI mitigated uv map and the corresponding dirty map, respectively. It can be seen that the spots contaminated by the Cygnus region have been excised in Fig.13. However, the two brightest radio sources, Cas A and Cygnus A, can still be found in the sky map (Fig.14), which are the result of the sidelobe leakage of the array.

6 DISCUSSION AND CONCLUSIONS

Low frequency radio astronomy, (to be) equipped with interferometers like SKA and data processing using cutting-edge technologies, has entered a golden era of development. It will revolutionize our understanding of the universe including future discoveries of the dark ages, cosmic dawn and EoR. Low frequency astronomy will also open up a new window for time domain research such as pulsar timing and high precision tests of gravity because of its large field of view and unprecedented high sensitivity. Yet, these ambitious sciences are built on the promise of a perfect mitigation of RFI including sky noise in low frequency radio observations. Indeed, even if we detect and excise all the man-made, terrestrial RFI, the cosmological signal may still be hidden in Galactic and extragalactic radio backgrounds. Many sophisticated methods and techniques should be explored to guarantee that the sky noise can be suppressed to the level of ~ 1 mK.

Using real 21CMA observations at 50-200 MHz, we have demonstrated how RFI is detected and mitigated with four different approaches: (1) Identify and flag all the time-varying events and sparks with high time and frequency resolutions. It is advantageous to apply this task during the data acquisition phase in real time, although one can also do the job in data post processing to ensure the maximum efficiency of data acquisition. With the fast development and wide application of GPU and FPGA related technology, real-time detection of RFI with unprecedented high efficiency has become possible for the next generation low frequency radio facilities. (2) Set a proper threshold to excise all the flagged data in the contaminated areas and even adjacent frequency channels. (3) Mitigate all the non-Gaussian features in terms of the criterion defined by mean and standard deviation. Using the visibility correlation coefficient instead of conventional visibility would improve the accuracy of RFI detection although it leads to a decreasing efficiency of data acquisition. (4) Detect and remove all bright Galactic and extragalactic radio sources both in the field of view and from the leakage of sidelobes. This last point may also be the last barrier to the detection of a cosmological signal from the dark ages and EoR. State-of-the-art algorithms developed in recent years seem to be very successful for removals of bright radio foregrounds.

While current low frequency radio facilities including the forthcoming SKA are sited in remote areas, any terrestrial radio telescopes at low frequencies suffer from at least two types of RFI contamination: (1) FM and TV broadcasting scattered by meteor trails and (2) satellite communications. This even does not account for the ionospheric effect on radio interferometric observations. An ideal site to do low frequency radio astronomy especially for the exploration of the dark ages, is the far side of the Moon. There are several ambitious projects that are being planned, either deploying radio telescopes on the dark side of the Moon or sending detectors into lunar orbit (e.g. DARE (Genova et al., 2015); a dedicated space-based ultra-long wavelength array (Rajan et al. 2015); Chang'e-5; etc.). If one observes the radio sky from the dark side of the Moon, Galactic and extragalactic radiation will be the only sources of contamination, with time-invariant power and a featureless spectrum like thermal noise. Many of the present RFI detection and mitigation methods for highly time-varying events and sparks would become obsolete. That will be the next milestone for low frequency radio astronomy.

Acknowledgements This work was partially supported by the National Natural Science Foundation of China (Grant No. 11433002). QZ acknowledges the support by a Marsden Fund grant in New Zealand.

References

- Alonso, D., Bull, P., Ferreira P. G., & Santos, M. G., 2015, MNRAS, 447, 400
- Amy, S. W., & Large, M. I., 1990, PASA, 8, 308
- Ardouin, D., et al., 2011, Astropart. Phys., 34, 717
- Bowman, J. D., et al., 2007, AJ, 133, 1505
- Bracewell, R., N., & Thompson, A. R., 1973, ApJ, 182, 77
- Genova, A. L., et al., 2015, arXiv:1504.00410
- Haslam, C. G. T., Salter, C. J., Stoffel, H., & Wilson, W. E., 1982, A&AS, 47, 1
- Henning, P. et al., 2010, in Proceedings of the ISKAF2010 Science Meeting, 24 (arXiv:1009.0666)
- Koopmans, L. V. E., et al., 2015, arXiv:1505.07568
- Neben, A. R. et al., 2015, Radio Science, 50, 614
- Noordam, J. E. & de Bruyn A. G., 1982, Nature, 299, 597
- Offringa, A. R., et al., 2013, A&A, 549, 11
- Offringa, A. R., et al., 2015, PASA, 32, e008
- Parsons, A. R., et al., 2014, ApJ, 788, 106
- Pober, J. C., et al., 2013, ApJ, 768, L36
- Rajan, R. T., Boonstra A.-J., Bentum, M., Klein-Wolt, M., Belien, F., Arts, M., Saks, N., & van der Veen, A.-J., 2015, arXiv:1505.04711
- Schwab, F.R., 1984, AJ, 89, 1076
- Taylor, G. B., 2012, JAI, 1, 1250004
- Tegmark, M., 2010, Phys. Rev. D, 82, 103501
- Zheng, Q., Wu, X.-P., Gu, J.-H., Wang, J., & Xu, H., 2012, ApJ, 758, L24
- Zheng, Q., et al. 2016, ApJ, to be submitted

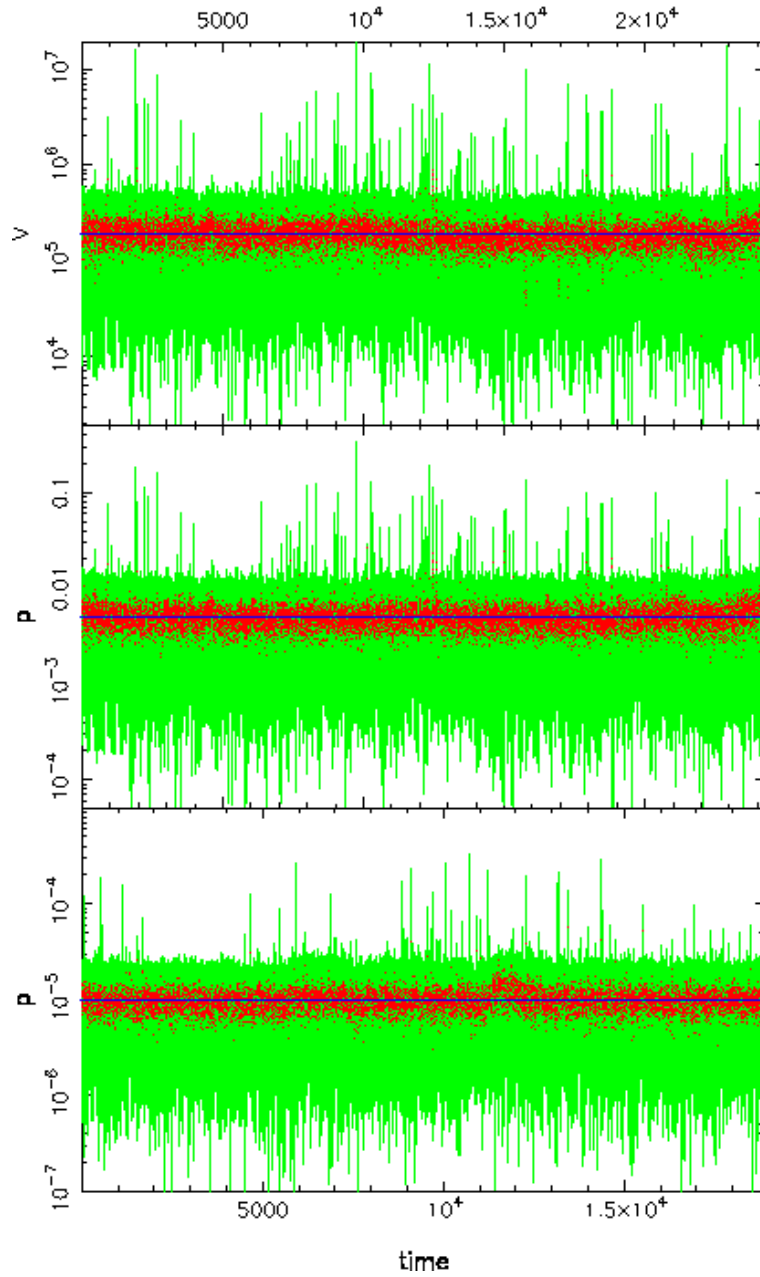


Fig. 8 Visibility power $|V_{E01E20}|$ (top), visibility correlation coefficient power $|p_{E01E20}|$ with data post processing approach (middle), and $|p_{E01E20}|$ with real-time operation (bottom). The central frequency is 102 MHz with a bandwidth of 0.1 MHz. The average among different channels at a given timestep is represented by red points, and the average over the whole integration time is indicated by a blue line.

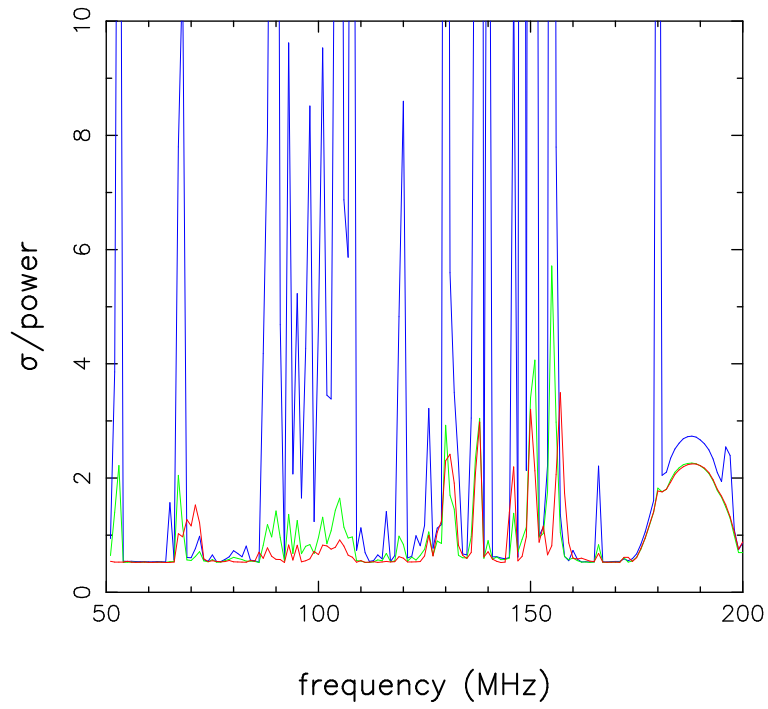


Fig. 9 Comparisons of data dispersion, represented by the ratio of standard deviation to mean value for three different approaches. The blue line represents V_{E01E20} ; the green line represents p_{E01E20} with data post processing; and the red line represents real-time p_{E01E20} .

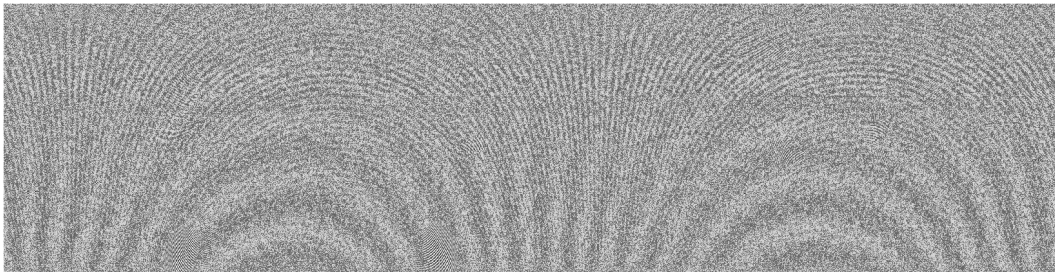


Fig. 10 The waterfall plot of the real part of visibility function V_{E01E20} spanning over 24 hours along the horizontal axis. The vertical axis represents frequency running from 50 MHz (top) to 200 MHz (bottom).

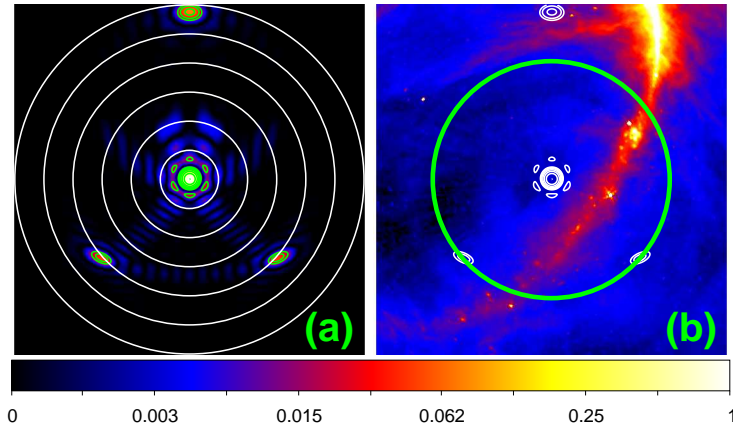


Fig. 11 The beam pattern of the 21CMA at $\nu = 150$ MHz (a) overlaid on the sky map of Haslam et al. 1982 for 408 MHz (b). An annulus with a diameter of 10 degrees indicates the area shown (a). The green circle in (b) indicates the locus of diurnal motion of the Galactic region that passes through the sidelobes of the 21CMA.

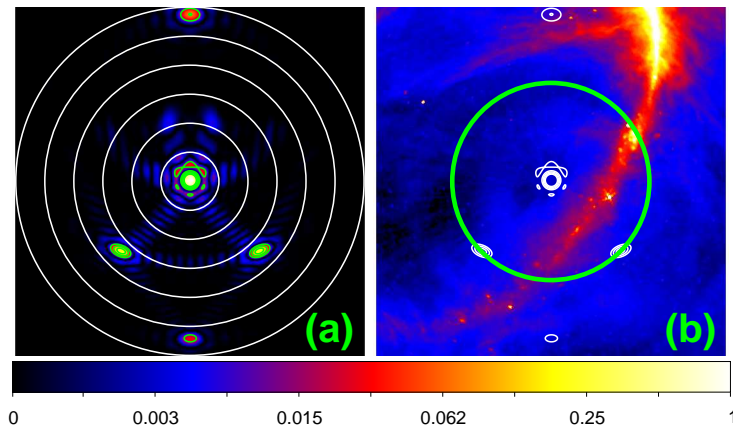


Fig. 12 The same as Fig.11 but for $\nu = 180$ MHz. The diurnal motion of the Cygnus region traces a circle with a radius of $\sim 45^\circ$ from NCP, which enables the sidelobes to ‘see’ the Cygnus region twice per day with an interval of 6 hours. Another bright spot on the Galactic plane and inside the circle is Cas A, the brightest supernova remnant in the radio sky.

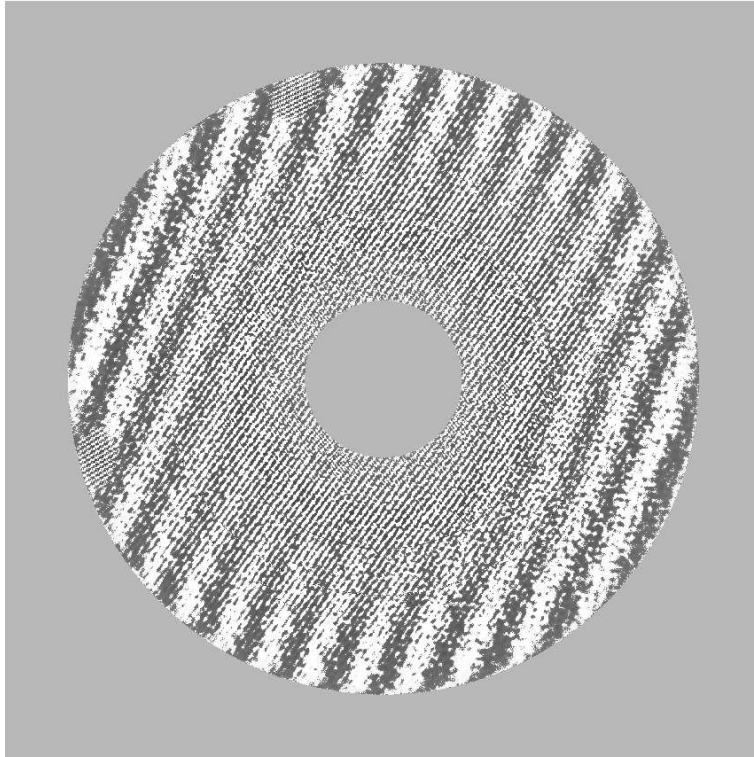


Fig. 13 The 24 hour uv coverage of E01E20 after RFI is mitigated. Frequency runs outward from 50 MHz to 200 MHz. Two gray spots correspond to the sidelobe leakages of the Cygnus region in the Milky Way. The gray ring near 137 MHz is due to ORBCOMM satellites.

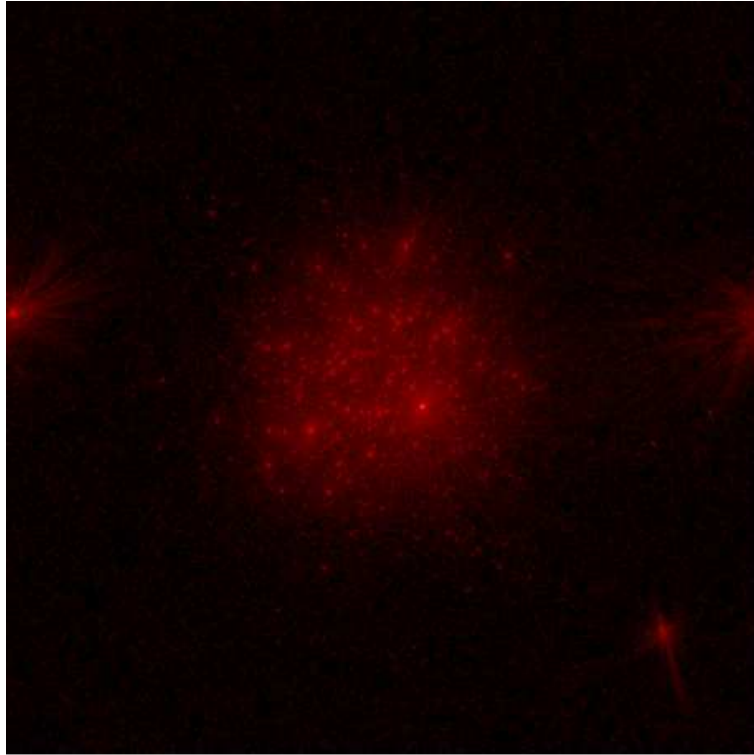


Fig. 14 The dirty map of the NCP region observed with 21CMA - an FFT of the uv map in Fig.13. A large field of $60^\circ \times 60^\circ$ is chosen to include the two brightest radio sources in the sky, Cas A (left) and Cygnus A (lower right), which are the result of the sidelobe leakage due to the regular spacings of the 21CMA antennas. No correction is made for spatial response function of the 21CMA antennas.